catalysts

MDPI

Article

Effect of Ba/Ce Ratio on the Structure and Performance of Pt-Based Catalysts: Correlation Between Physicochemical Properties and NO_x Storage–Reduction Activity

Dongxia Yang [1,2,3,*], Yanxing Sun [1], Tingting Zheng [1,2,3], Lv Guo [1], Yao Huang [1], Junchen Du [1,2,3], Xinyue Wang [4] and Ping Ning [5,*]

[1] State-Local Joint Engineering Research Center of Precious Metal Catalytic Technology and Application, Kunming Sino-Platinum Metals Catalysts Co., Ltd., Kunming 650106, China
[2] State Key Laboratory of Precious Metal Functional Materials, Kunming Institute of Precious Metals, Kunming 650106, China
[3] Yunnan Precious Metal Laboratory Co., Ltd., Kunming 650106, China
[4] Faculty of Material Science and Engineering, Kunming University of Science and Technology, Kunming 650500, China; xwang@kust.edu.cn
[5] Faculty of Environmental Science and Engineering, Kunming University of Science and Technology, Kunming 650500, China
* Correspondence: doris.yang@spmcatalyst.com (D.Y.); ningping58@sina.com (P.N.)

Abstract

The continuous tightening of emission regulations and the escalating costs of palladium (Pd) and rhodium (Rh) have renewed interest in platinum (Pt)-based three-way catalysts (TWCs) as cost-effective alternatives for gasoline aftertreatment. However, despite extensive studies on Pt/CeO_2 and Pt/Ba-based formulations, the cooperative roles of Ba and Ce and, in particular, the fundamental influence of the Ba/Ce ratio on oxygen mobility, NO_x storage behavior, and Pt–support interactions remain poorly understood. In this work, we address this gap by systematically tuning the Ba/Ce molar ratio in a series of $Pt–Ba–Ce/Al_2O_3$ catalysts prepared from $Ba(CH_3COO)_2$ and CeO_2 precursors, and evaluating their structure–function relationships in both fresh and hydrothermally aged states. Through comprehensive characterization (N_2 physisorption, XRD, XPS, H_2-TPR, NO_x-TPD, SEM, CO pulse adsorption, and dynamic light-off testing), we establish previously unrecognized correlations between Ba/Ce ratio–dependent structural evolution and TWC performance. The results reveal that the Ba/Ce ratio exerts a decisive control over catalyst textural properties, Pt dispersion, and interfacial $Pt–CeO_2$ oxygen species. Low Ba/Ce ratios uniquely promote Pt–Ce interfacial oxygen and O_2 spillover—providing a new mechanistic basis for enhanced low-temperature oxidation and reduction reactions—while higher Ba loading selectively drives $BaCO_3$ formation and boosts NO_x storage capacity. A clear volcano-type dependence of NO_x storage on the Ba/Ce ratio is demonstrated for the first time. Hydrothermal aging at 850 °C induces PtO_x decomposition, $BaCO_3–Al_2O_3$ solid-state reactions forming inactive $BaAl_2O_4$, and Pt sintering, collectively suppressing Pt–Ce interactions and reducing TWC activity. Importantly, an optimized Ba/Ce ratio is shown to mitigate these degradation pathways, offering a new design principle for thermally durable Pt-based TWCs. Overall, this study provides new mechanistic insight into Ba–Ce cooperative effects, establishes the Ba/Ce ratio as a critical and previously overlooked parameter governing Pt–support interactions and NO_x storage, and presents a rational strategy for designing cost-effective, hydrothermally robust Pt-based alternatives to Pd/Rh commercial TWCs.

Check for updates

Academic Editor: Leonarda Liotta

Received: 10 November 2025
Revised: 15 December 2025
Accepted: 19 December 2025
Published: 26 December 2025

Copyright: © 2025 by the authors. Licensee MDPI, Basel, Switzerland. This article is an open access article distributed under the terms and conditions of the Creative Commons Attribution (CC BY) license.

Keywords: three-way catalyst (TWC); NO_x storage–reduction (NSR) catalysts; Ba/Ce ratio

1. Introduction

Since the invention of the oxygen sensor by Bosch in 1976, the combination of electronically controlled fuel injection and three-way catalysts (TWCs) has made a profound contribution to the simultaneous abatement of CO, HC, and NO_x emissions from gasoline engines [1]. With the continuous tightening of emission regulations and the dramatic fluctuations in precious metal prices, commercial TWCs have gradually shifted from the initial Pt/Rh formulations to Pd/Rh-based catalysts [2]. However, since 2019, the prices of Pd and Rh have surged significantly, with Pd reaching nearly 2000 USD/oz and Rh approaching 8500 USD/oz. In contrast, Pt remains approximately one-third the price of Pd and one-tenth that of Rh, which makes it an economically attractive alternative. Nevertheless, systematic studies on Pt-only TWCs remain relatively limited [3].

NO_x storage–reduction (NSR) catalysts, typically represented by $Pt/BaO/Al_2O_3$, are often regarded as a hybrid between conventional TWCs and alkaline storage components [4,5]. Although NSR catalysts are highly effective for NO_x abatement under lean conditions, their performance in CO and HC oxidation under rich conditions is inadequate. In real automotive exhaust conditions, the catalyst operates under dynamic lean–rich cycling near the stoichiometric air–fuel ratio. Thus, Ce-based oxygen storage materials are frequently incorporated to regulate the catalyst operation window due to their ability to store oxygen under lean conditions and release it under rich conditions [6]. CeO_2 not only provides excellent oxygen storage–release capacity (OSC) but also enhances the dispersion of precious metals, promotes water–gas shift and steam reforming reactions, and introduces basicity beneficial for NO_x storage [7–9]. On the other hand, Ba plays a crucial role as an alkaline NO_x storage medium, and its incorporation into TWCs has also been reported to improve overall activity, thermal stability, and hydrothermal durability [5,6,10].

Despite the individual advantages of Ba- and Ce-containing components, their coexistence within the same catalyst system introduces complex and often competing interactions. Studies have demonstrated that the Ba/Ce ratio critically determines catalyst microstructure, storage capacity, and durability [11,12]. For instance, CeO_2 dispersed on Al_2O_3 provides highly dispersed $BaCO_3$ domains that are beneficial for NO_x storage, whereas excess Ba tends to form stable but catalytically inert $BaAl_2O_4$ upon hydrothermal aging [13]. Conversely, simultaneous modification of Pd or Pt catalysts with both BaO and CeO_2 can sometimes lead to competitive effects that suppress their individual beneficial functions [14,15]. These findings highlight the necessity of systematically optimizing the Ba/Ce ratio to balance storage capacity, redox properties, and structural stability under realistic operating conditions. However, existing reports primarily describe these interactions qualitatively, without establishing quantitative or mechanistic relationships.

Nevertheless, despite these insights, a comprehensive understanding of how the Ba/Ce ratio governs the physicochemical evolution, Pt–support interactions, NO_x storage behavior, and three-way catalytic performance of Pt-based formulations remains largely unexplored. Existing studies typically vary Ba or Ce loading individually, focus on Pd-based catalysts, or examine storage and oxygen materials in isolation. As a result, the cooperative or competitive interplay between Ba and Ce under realistic TWC conditions—particularly during hydrothermal aging—remains insufficiently understood. In particular, the mechanistic links among Ba/Ce ratio–dependent oxygen mobility, Pt dispersion, $BaCO_3$ domain

evolution, and performance deterioration during high-temperature aging have not yet been established, leaving a critical gap in rational catalyst design.

In this study, we focus on Pt-based Ba–Ce/Al_2O_3 catalysts prepared by introducing Ba via $Ba(CH_3COO)_2$ precursors and Ce via solid CeO_2 powders. A series of fresh and hydrothermally aged xBa–yCe-PA catalysts with different molar Ba/Ce ratios were synthesized and comprehensively characterized by N_2 physisorption, XRD, XPS, H_2-TPR, SEM, NO_x-TPD, CO pulse adsorption, NO_x storage tests, and dynamic light-off evaluations. The objective is to unravel the structure–performance relationships of Pt-based catalysts, elucidate the role of Ba/Ce interactions in determining NO_x storage and three-way conversion activity, and clarify the evolutionary mechanisms during hydrothermal aging. This systematic investigation provides insights into designing cost-effective, thermally durable Pt-based catalysts as potential alternatives to Pd/Rh-dominated commercial TWCs.

2. Results and Discussion

2.1. N_2 Physisorption Analysis: BET Surface Area and Pore Structure Characterization

The N_2 adsorption–desorption isotherms and pore size distributions of the catalysts with different Ba/Ce ratios are shown in Figure 1, and the corresponding textural parameters are summarized in Table 1. All samples exhibit type IV isotherms with H3-type hysteresis loops, characteristic of mesoporous materials, indicating the preservation of mesoporous structures upon Ba and Ce incorporation [16].

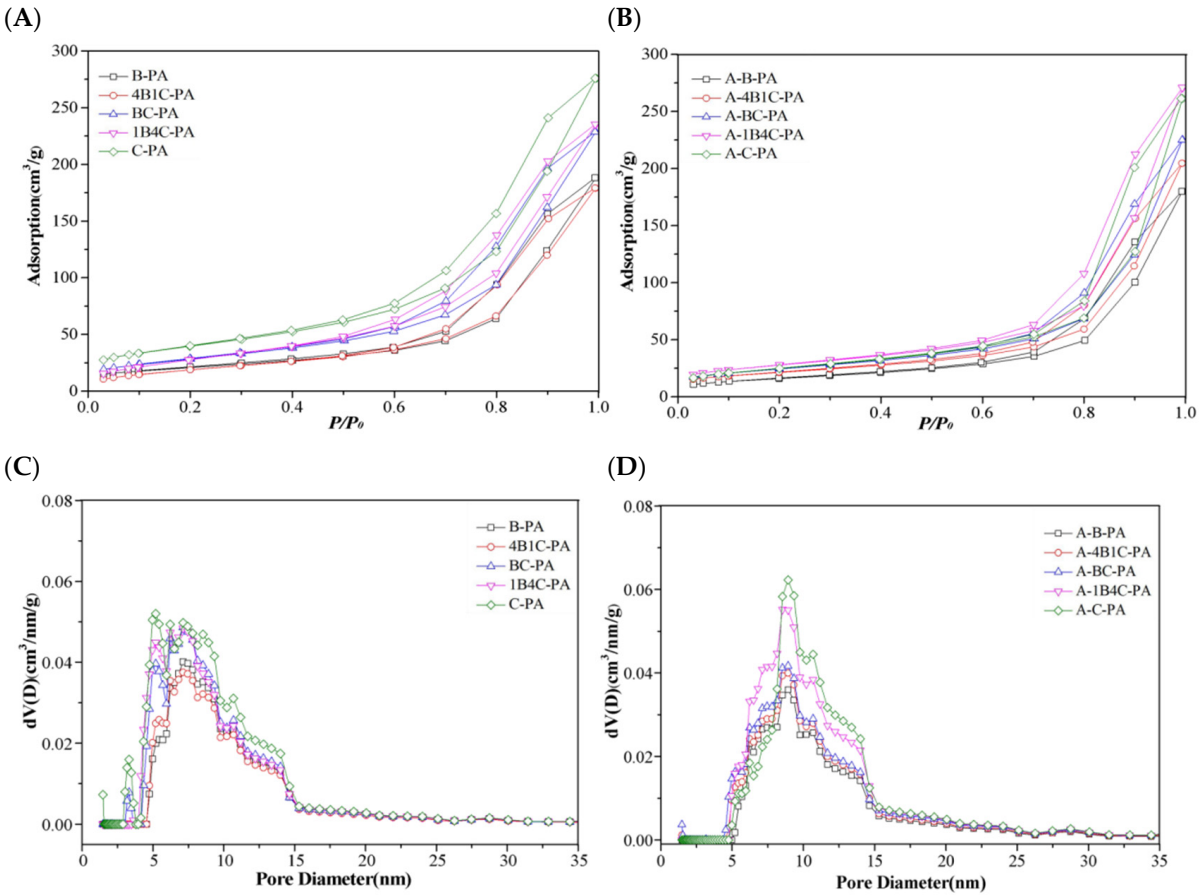


Figure 1. N_2 Adsorption–Desorption Isotherms and Pore Size Distributions of Catalysts with Different Ba/Ce Ratios: (**A**,**C**) Fresh Catalysts and (**B**,**D**) Hydrothermally Aged Catalysts.

Table 1. Specific surface, pore volume and mean pore diameters.

Sample	Specific Surface Area (m^2/g)	Pore Volume (mL/g)	Average Pore Diameter (nm)
La_2O_3–Al_2O_3	143	0.36	7.2
CeO_2	141	0.29	7.6
B-PA	74	0.29	6.9
4B1C-PA	72	0.28	6.6
BC-PA	102	0.35	6.3
1B4C-PA	104	0.35	6.4
C-PA	142	0.43	5.8
A-B-PA	58	0.28	7.0
A-4B1C-PA	76	0.32	6.7
A-BC-PA	87	0.35	6.4
A-1B4C-PA	99	0.42	6.7
A-C-PA	90	0.41	6.8

Among the fresh catalysts (Figure 1A and Table 1), C-PA displays the largest BET surface area (142 m^2/g) and pore volume (0.43 mL/g), accompanied by the smallest average pore diameter (1.20 nm), suggesting the development of abundant accessible mesopores that could enhance catalytic activity. In contrast, B-PA and 4B1C-PA exhibit significantly lower surface areas (74 and 72 m^2/g, respectively) and reduced pore volumes (0.29 and 0.28 mL/g), consistent with partial pore blockage induced by Ba loading. BC-PA and 1B4C-PA maintain intermediate surface areas (~10^2–10^4 m^2/g) with pore diameters around 1.38–1.40 nm, reflecting a balance between structural stability and microporosity.

After hydrothermal aging (Figure 1B,D), most samples undergo a noticeable reduction in surface area and pore volume, in line with pore narrowing and framework densification. For example, A-B-PA shows a surface area of only 58 m^2/g and a pore volume of 0.2 mL/g, while A-4B1C-PA and A-BC-PA retain slightly higher values (76 and 87 m^2/g, respectively). Interestingly, A-C-PA preserves a relatively high surface area (90 m^2/g) and pore volume (0.41 mL/g), indicating superior hydrothermal stability compared to Ba-rich compositions. The corresponding pore size distributions (Figure 1C,D) confirm that most mesopores are concentrated in the 2–5 nm range, with aged catalysts showing narrower distributions and reduced mesopore volumes [17].

Overall, the BET surface area and pore structure data highlight that Ce-rich catalysts (C-PA, A-C-PA) retain higher surface areas and mesopore accessibility, whereas Ba-rich systems (B-PA, A-B-PA) suffer from severe textural degradation upon hydrothermal aging. These trends align with previous reports that alkaline-earth dopants promote densification and sintering, while rare-earth oxides impart improved structural stability under hydrothermal conditions [17].

2.2. Phase Structure and Crystallite Size of the Catalyst

The XRD results (Figure 2) together with the crystallite size data (Table 2) provide critical insights into the structural evolution of the catalysts as a function of Ba/Ce ratio and hydrothermal aging. In fresh samples, the absence of detectable Pt diffraction peaks suggests that Pt species are either atomically dispersed or present as ultra-fine clusters (<5 nm), consistent with previous reports on Pt/CeO_2 and Pt/Al_2O_3 catalysts where high metal dispersion suppresses XRD detectability of Pt phases [18,19]. The observed strengthening of $BaCO_3$ reflections with increasing Ba content, alongside the attenuation of CeO_2 peaks, indicates that Ba enrichment suppresses ceria crystallinity, while Ce-rich samples maintain smaller CeO_2 crystallites (Table 2), thereby enhancing oxygen storage and metal–support interactions [20].

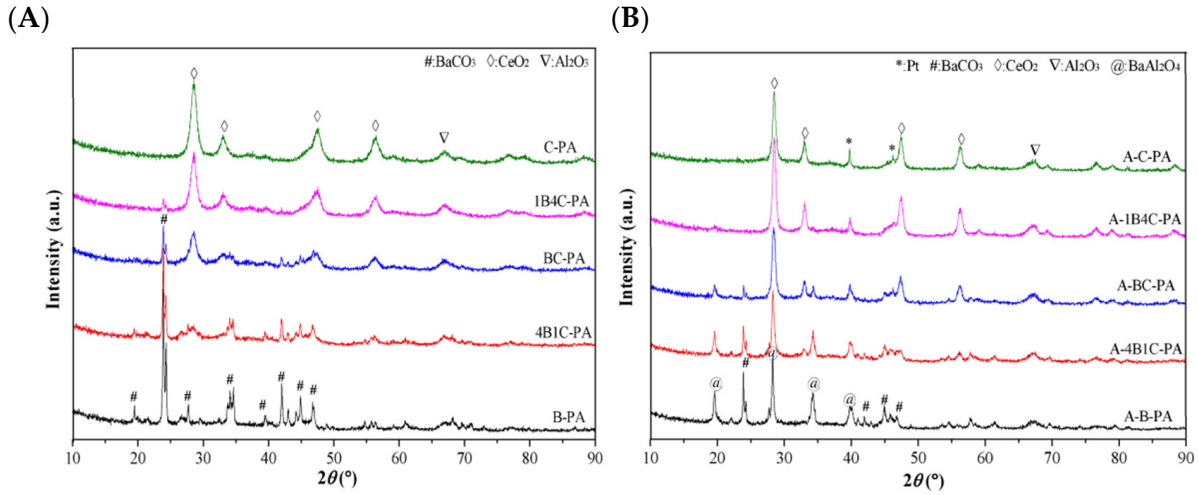


Figure 2. XRD patterns of catalysts with different Ba/Ce ratios: (**A**) fresh samples; (**B**) hydrothermally aged samples.

Table 2. Physical parameters of fresh and hydrothermally aged catalysts with varying Ba/Ce ratios.

Sample	CeO_2 Crystallite Size (nm)	$BaCO_3$ Crystallite Size (nm)	Pt Crystallite Size (nm)	Pt Particle Size (nm)	Pt Dispersion (%)	Pt Loading (wt.%)
B-PA	–	31.5	–	2.83	29.90	0.90
4B1C-PA	19.2	30.0	–	2.11	40.18	1.01
BC-PA	18.1	29.6	–	1.92	44.01	1.04
1B4C-PA	10.8	23.2	–	1.89	45.46	1.03
C-PA	11.7	–	–	1.34	63.25	1.00
A-B-PA	–	28.1	16.0	11.53	7.35	0.89
A-4B1C-PA	16.0	27.9	14.9	10.83	7.79	0.94
A-BC-PA	17.8	37.6	20.3	19.61	6.97	0.88
A-1B4C-PA	17.9	24.1	32.85	32.85	2.58	0.87
A-C-PA	23.4	–	48.8	44.60	1.90	0.94

Upon hydrothermal aging at 850 °C, distinct diffraction peaks corresponding to $BaAl_2O_4$ and metallic Pt emerge, highlighting two critical processes, firstly, solid-state reactions between $BaCO_3$ and Al_2O_3 leading to the formation of $BaAl_2O_4$, which has been previously reported as a thermally stable but catalytically less active phase; secondly, growth of Pt and CeO_2 crystallites, confirming sintering and agglomeration under high-temperature conditions [21]. Notably, the CeO_2 peaks become sharper after aging, reflecting increased crystallinity and particle size, which may reduce oxygen vacancy concentration and weaken redox capacity [22].

It should be noted that although the XRD-derived Pt crystallite size after aging becomes larger than that of CeO_2, this phenomenon is fully consistent with the known hydrothermal degradation mechanism of Pt-based TWCs, where PtOx decomposition and particle coalescence reduce the Pt–CeO_2 interfacial contact. Such structural evolution naturally leads to a decline in catalytic activity, which is indeed observed in our aged samples. Moreover, XRD crystallite size reflects the coherent diffraction domain and typically overestimates the surface-exposed Pt nanoparticle size; therefore, the correlation between XRD-derived crystallite dimensions and catalytic performance is not strictly linear.

Interestingly, the correlation between Ba/Ce ratio and Pt dispersion is not strictly linear. While Ba-rich systems tend to promote Pt agglomeration due to weaker metal–support anchoring, the A-4B1C-PA catalyst exhibits the smallest Pt crystallite size and the highest Pt dispersion after aging, suggesting that an optimal Ba/Ce ratio can stabilize Pt species

and inhibit sintering. This finding is consistent with prior studies that demonstrated synergistic effects of Ba and Ce in maintaining dispersion of noble metals under severe aging conditions [23,24]. Thus, tuning the Ba/Ce ratio offers a promising route to balance structural stability and catalytic activity by suppressing the sintering of active species while maintaining oxygen storage properties.

2.3. Morphology and Textural Analysis

The SEM images (Figure 3) provide further morphological evidence to support the crystallographic and textural properties obtained from XRD and N_2 physisorption analyses. For the fresh catalysts, a clear trend is observed with increasing Ce content, the particles gradually become smaller and more fragmented. For instance, C-PA exhibits the most finely divided morphology, consistent with its highest BET surface area (142.2 m^2/g) and pore volume (0.428 mL/g) among the series (Table 1). In contrast, Ba-rich samples such as 4B1C-PA and BC-PA display larger, more aggregated particles, correlating with their lower surface areas (~7^2–10^2 m^2/g) and smaller pore volumes. These results confirm that Ce addition inhibits crystallite growth and enhances mesoporosity, thereby improving textural properties and dispersion of the active phase. This finding is in agreement with previous studies reporting that CeO_2 acts as a structural promoter by generating oxygen vacancies and stabilizing smaller crystallites [22].

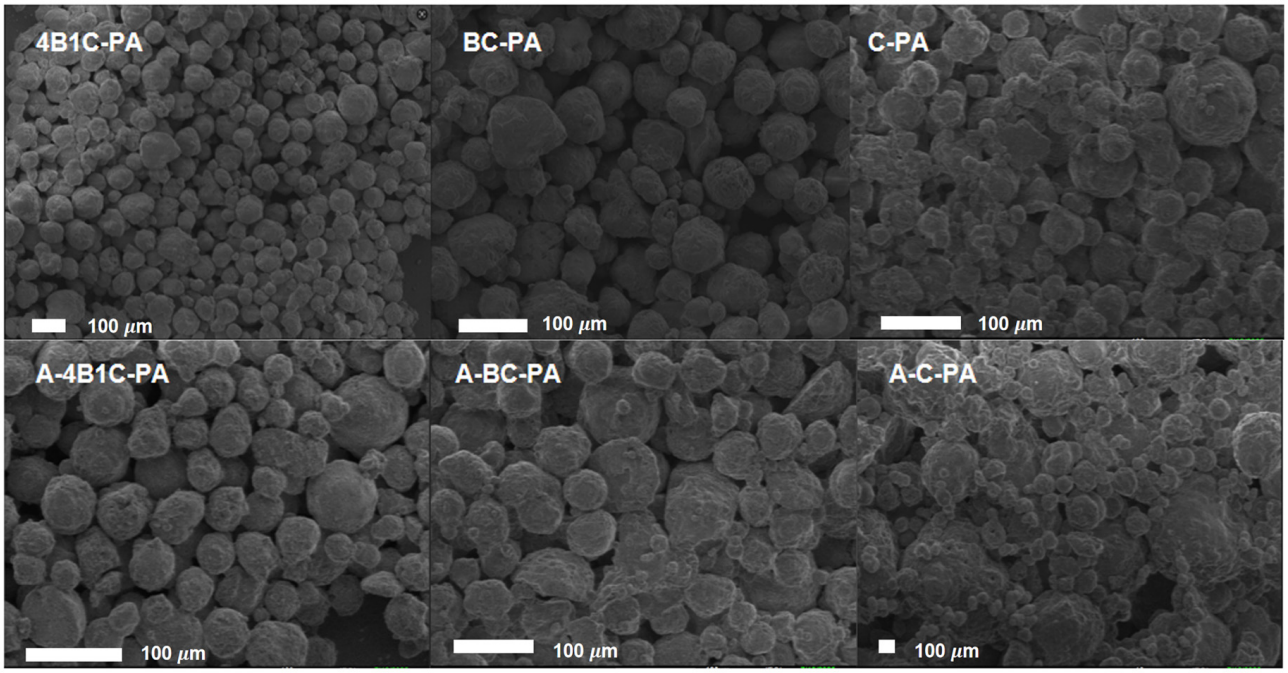


Figure 3. SEM images of fresh (**top**) and aged (**bottom**) catalysts with varying Ba/Ce ratios.

After hydrothermal aging, all samples show significant particle coarsening and agglomeration. The particle boundaries become smoother, and the overall morphology appears more sintered compared to the fresh state. Nevertheless, Ce-rich aged catalysts (e.g., A-C-PA and A-BC-PA) still retain relatively smaller and less compact particles compared to their Ba-rich counterparts (e.g., A-4B1C-PA). This observation is consistent with the XRD-derived crystallite sizes, where CeO_2 crystallite growth was less pronounced (from ~10–19 nm in fresh to ~16–23 nm in aged samples), while $BaCO_3$ crystallites underwent more severe enlargement (from ~23–31 nm to ~28–38 nm). The N_2 adsorption data also corroborate this trend, showing that Ce-rich catalysts preserved higher pore volume and surface area after aging relative to Ba-rich samples.

2.4. Electronic Properties of the Active Metal Species

To investigate the influence of the Ba/Ce ratio on the electronic state of the active metal species, X-ray photoelectron spectroscopy (XPS) was performed on the catalysts. Because the Pt 4f region (78–70 eV) overlaps strongly with the Al 2p signal from the La–Al_2O_3 support, the Pt 4d region (340–310 eV) was selected for analysis (Figure 4). However, due to the intrinsically weak Pt 4d cross section and the relatively low Pt loading, the Pt 4d spectra exhibit a limited signal-to-noise ratio. As a result, only qualitative trends in the Pt $4d_5/_2$ binding energy were evaluated, and no attempt was made to quantitatively analyze the Pt 4d spin–orbit splitting. The apparent variation in the energy separation between the Pt $4d_5/_2$ and $4d_3/_2$ components among different samples is therefore attributed to spectral noise rather than true chemical differences, and the discussion is restricted to the more reliable Pt $4d_5/_2$ peak position.

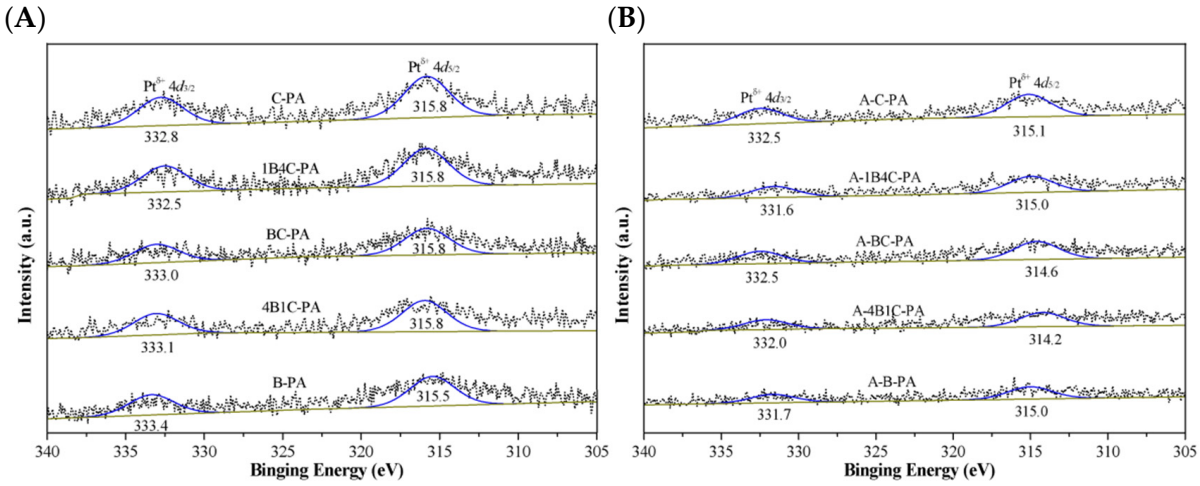


Figure 4. XPS Pt 4d spectra of (**A**) fresh and (**B**) hydrothermally aged catalysts with varying Ba/Ce ratios.

For the fresh catalysts, the Pt $4d_5/_2$ binding energy gradually increases from 315.5 eV in B-PA to 315.8 eV in Ce-rich samples, indicating enhanced electronic interaction between Pt and CeO_2. This shift is consistent with electron transfer from Pt to CeO_2, which modifies the Pt d-band and strengthens metal–support interactions, in agreement with previous reports on Pt/CeO_2 systems [22,25].

Upon hydrothermal aging at 850 °C, all catalysts show a decrease in Pt $4d_5/_2$ binding energy, reflecting the partial reduction of PtOx species and the sintering-induced decrease in surface-exposed Pt atoms [26]. Importantly, the reduced Pt signal intensity arises from loss of surface accessibility and not from Pt volatilization, as Pt is non-volatile under the present conditions and PtOx decomposition removes only oxygen while preserving Pt mass. Within the aged catalysts, the Pt $4d_5/_2$ binding energy increases with CeO_2 content, indicating renewed electronic interaction between Pt and Ce after structural reconstruction during aging. This trend further confirms that CeO_2 plays the dominant role in governing Pt electronic properties in the Pt–Ba–Ce–Al system [27,28].

2.5. Reducibility of Catalyst Components

Figure 5 shows the H_2-TPR profiles of the catalysts, and the quantitative parameters are summarized in Table 3. In Pt–Ce–Ba–Al systems, only PtOx species and ceria-derived oxygen are reducible in the temperature range probed, whereas Ba-containing phases ($BaCO_3$, BaO, $BaAl_2O_4$) are non-reducible. Thus, H_2 consumption reflects Pt- and Ce-related processes, while any interaction of H_2 with carbonates corresponds to hydrogena-

tion/decomposition, producing CO_2 rather than oxygen removal. Because the TPR setup did not include a CO_2 trap, CO_2–TCD interference is possible and has been considered in the analysis [20,29].

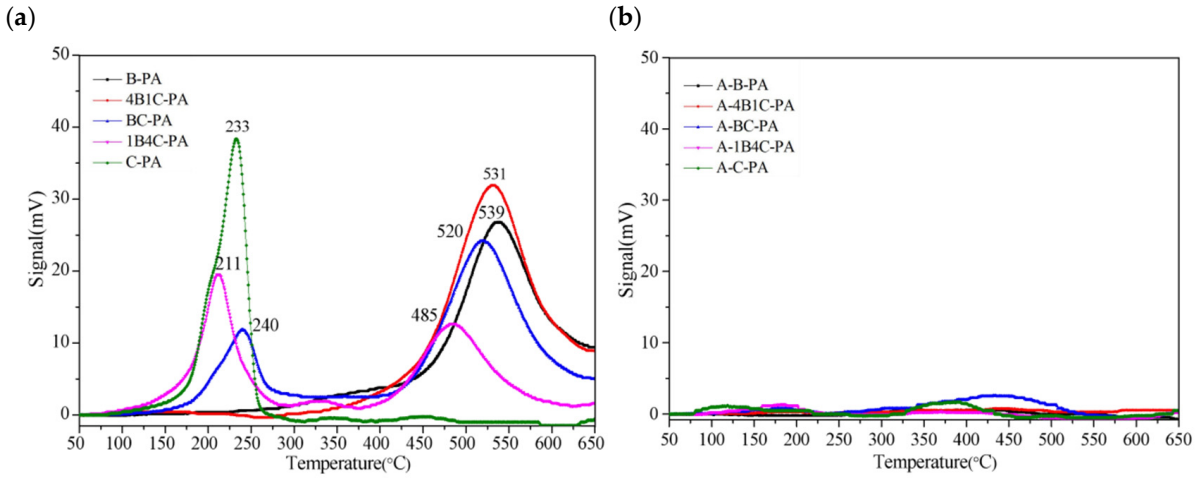


Figure 5. H_2-TPR profiles of catalysts with varying Ba/Ce ratios: (**a**) fresh samples; (**b**) hydrothermally aged samples.

Table 3. Quantitative H_2-TPR analysis of catalysts with varying Ba/Ce ratios.

Sample	Low-Temperature Reduction Peak Temperature (°C)	Low-Temperature Reduction Peak Area (CPS)	High-Temperature Reduction Peak Temperature (°C)	High-Temperature Reduction Peak Area (CPS)
B-PA	-	-	539	2624.14
4B1C-PA	-	-	531	3550.72
BC-PA	240	688.85	520	2167.84
1B4C-PA	211	868.9	485	962.6
C-PA	233	1611.16	-	-

Fresh catalysts exhibit a distinct low-temperature peak (210–240 °C), attributable to the reduction of PtOx and interfacial Pt–O–Ce species. The intensity of this feature increases with Ce loading, indicating a larger population of labile oxygen species associated with highly dispersed Pt–Ce interfaces. A second peak at 480–540 °C arises from deeper ceria lattice oxygen. Its shift to higher temperature with increasing Ba content reflects reduced Pt–Ce contact and partial ceria surface coverage by $BaCO_3$, consistent with the larger ceria crystallite sizes in Ba-rich samples [26].

In Ba-rich formulations, carbonate hydrogenation may contribute to broad or distorted high-temperature signals, further emphasizing the need for cautious interpretation of H_2 consumption in these samples [30,31].

Hydrothermally aged catalysts show strongly attenuated or nearly vanished reduction peaks [32]. This loss of reducibility is attributed to Pt sintering (eliminating PtOx and Pt–Ce interfacial oxygen), ceria coarsening, and partial transformation of $BaCO_3$ into non-reducible $BaAl_2O_4$ [33]. Enlarged TPR profiles and quantified peak areas confirm the drastic decrease in hydrogen uptake, indicating a significant reduction in redox-active oxygen species [34].

Overall, these results demonstrate that the Ba/Ce ratio governs the reducibility of the fresh catalysts—Ce promoting low-temperature redox activity and Ba suppressing ceria reduction—while hydrothermal aging deactivates both processes through structural reconstruction of Pt, CeO_2, and Ba phases.

2.6. Interactions Among Catalyst Components

In Pt–Ba–Al-based lean NO_x trap (LNT) catalysts, NO_x storage proceeds primarily through the formation of nitrites and nitrates on $BaCO_3$, which is the dominant barium-containing phase under realistic exhaust conditions [35,36]. Unlike idealized $Pt/BaO/Al_2O_3$ systems discussed in early studies, $BaCO_3$ does not decompose to BaO under our operating temperatures (≤550 °C) or under hydrothermal aging conditions (850 °C, 8% O_2 and 8% CO_2). Therefore, $BaCO_3$—not BaO—is the actual NO_x storage medium in the present catalysts.

During the lean phase, NO is oxidized on Pt sites to NO_2:

$$2NO + O_2 \rightarrow 2NO_2 \text{ (Pt-catalyzed)}$$

The generated NO_2 subsequently reacts with $BaCO_3$ to form nitrates via:

$$BaCO_3 + 2NO_2 \rightarrow Ba(NO_3)_2 + CO_2$$

$$BaCO_3 + 2NO_2 + ½O_2 \rightarrow Ba(NO_3)_2 + CO_2$$

These reactions constitute the dominant nitrate-formation pathway in $BaCO_3$-containing LNT catalysts, consistent with widely reported mechanisms for $Pt/BaCO_3/Al_2O_3$ systems. Nitrite intermediates may transiently form on Pt or CeO_2 surfaces, but nitrate formation on $BaCO_3$ is thermodynamically favored under typical exhaust conditions.

As nitrate accumulation progresses, NO_2 spillover from Pt and CeO_2 domains toward $BaCO_3$ storage sites takes place, enabling storage at sites located further away from Pt. The efficiency of this spillover process is strongly influenced by the spatial proximity of Pt to $BaCO_3$ and by the oxygen mobility of the support. Accordingly, NO_x-TPD profiles provide insights into both the strength of nitrate binding and the Pt–$BaCO_3$ domain connectivity.

During the subsequent rich phase, stored nitrate species decompose or are reduced by CO, H_2, or hydrocarbons to release NO, N_2, or NH_3, depending on temperature and gas composition. Nitrate decomposition occurs preferentially at $BaCO_3$ sites closer to Pt because reductants activate more readily at Pt and diffuse outward via spillover mechanisms [37].

This $BaCO_3$-based mechanistic framework reflects the actual chemical environment of the catalysts studied here and provides a consistent explanation for the NO_x storage behaviors observed in both fresh and hydrothermally aged samples.

As shown in Figure 6, the fresh B-PA catalyst exhibits a NO_x desorption peak centered at 476 °C. After hydrothermal aging at 850 °C, the corresponding peak for A-B-PA shifts to 457 °C. This downward shift indicates that the stored NO_x species become less strongly bound upon aging, which can be ascribed to structural and chemical changes in the $BaCO_3$ domains and their environment. Hydrothermal treatment partially modifies and redistributes $BaCO_3$ and alters the proximity and electronic environment of Pt relative to Ba-containing storage sites, leading to less stable nitrate species that decompose at lower temperatures [38].

For the fresh catalysts, increasing the Ba/Ce ratio results in progressively higher desorption temperatures and larger peak areas (Figure 6A). This trend reflects the dual role of CeO_2. On the one hand, the introduction of CeO_2 enhances Pt–Ce interactions and oxygen mobility, which facilitates NO_x release and regeneration at lower temperatures, as evidenced by the lower desorption temperatures in Ce-rich samples. On the other hand, increasing Ce content dilutes or partially covers $BaCO_3$, thereby decreasing the number of available Ba-based storage sites and reducing the overall NO_x storage capacity. Consequently, Ce-rich catalysts exhibit improved low-temperature redox prop-

erties (consistent with H_2-TPR results) but weaker NO_x storage capacity compared with Ba-rich counterparts.

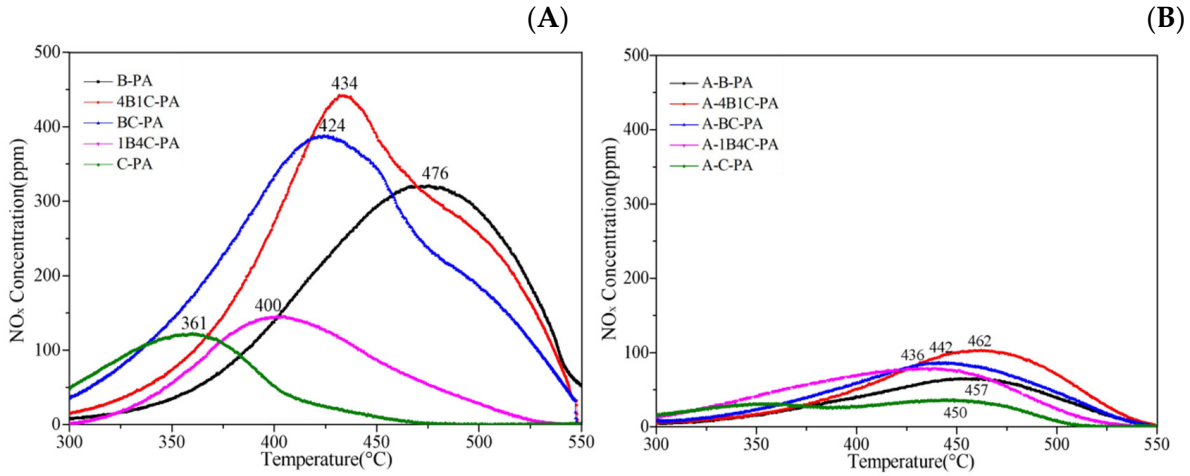


Figure 6. NO_x-TPD Spectra of (**A**) Fresh and (**B**) Aged Catalysts with Varying Ba/Ce Ratios.

After hydrothermal aging, all Ce-containing catalysts display markedly increased NO_x desorption temperatures (Figure 6B). This behavior can be rationalized by the combined effects of Pt sintering and aggregation, diminished Pt–CeO_2 charge transfer, and reduced oxygen mobility, which all hinder the regeneration of Ba-based nitrate species [34]. In addition, XRD results show that a fraction of $BaCO_3$ is converted into $BaAl_2O_4$ during aging, a thermodynamically stable and non-storage phase that weakens the effective Ba–Pt synergy. As a result, aged Ce-containing catalysts exhibit both reduced NO_x storage capacity and less efficient regeneration, underscoring the importance of optimizing the Ba/Ce ratio to balance storage ability and durability in LNT-type formulations.

The combined results from BET, XRD, XPS, H_2-TPR, NO_x-TPD, and SEM analyses reveal distinct structural roles of Ce and Ba in determining the redox and storage properties of the catalysts. In fresh samples, CeO_2 stabilizes PtOx species through strong metal–support interactions, forming Pt–O–Ce interfacial bonds that enhance oxygen mobility and low-temperature redox activity [22,26]. SEM and BET data confirm that Ce-rich catalysts (e.g., C-PA) possess smaller, more fragmented particles with higher surface areas, favoring Pt dispersion, whereas Ba-rich catalysts exhibit larger aggregated morphologies and higher NO_x storage capacity due to $BaCO_3$, but show weaker Pt–Ce interactions and reduced reducibility [34]. Upon hydrothermal aging at 850 °C, PtOx partially decomposes into lower-valent or metallic Pt species with pronounced particle growth (XPS, SEM), while $BaCO_3$ reacts with Al_2O_3 to form $BaAl_2O_4$, a stable but inert phase that diminishes high-temperature reducibility and NO_x storage. Concurrently, CeO_2 crystallite growth weakens Pt–CeO_2 interactions, leading to a loss of interfacial oxygen species and decreased oxygen mobility. Although some Pt–Ba proximity is observed after aging, it cannot compensate for the loss of Pt–Ce synergy. These results suggest a structural evolution pathway where Ce is crucial for stabilizing dispersed Pt and promoting oxygen mobility, while Ba contributes primarily to NO_x storage but facilitates sintering and inert phase formation under severe aging [23]. Optimizing the Ba/Ce ratio is therefore essential to balance redox activity and NO_x storage durability in practical LNT catalysts. The hydrothermal aging-induced evolution in the Ba–Ce–Pt–Al catalyst system shown in Figure 7.

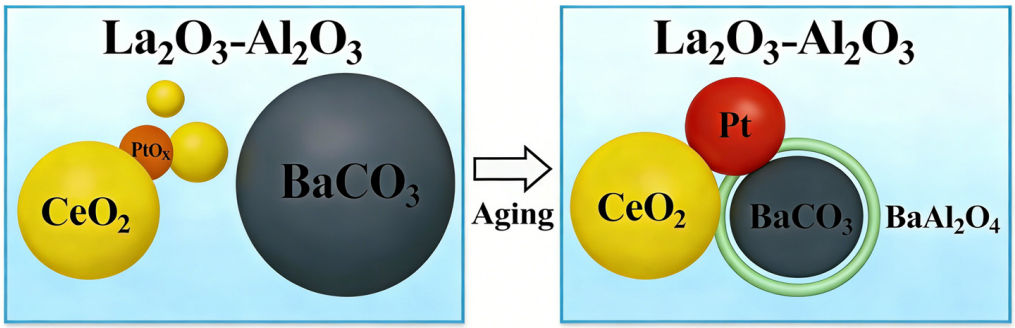


Figure 7. Schematic Illustration of Hydrothermal Aging-Induced Evolution in the Ba–Ce–Pt–Al Catalyst System.

2.7. NO_x Storage Properties of the Catalyst

Figure 8 shows the variation of NO_x concentration and NO_2/NO ratio over time during the NO_x storage process at 300 °C for catalysts with different Ba/Ce ratios. As observed in the initial phase after switching to a NO + O_2 + N_2 gas mixture, almost no NO_x is detected in the effluent, indicating that NO_x is rapidly and completely stored on the catalyst surface via the nitrite storage pathway. With increasing storage time, both the NO_x concentration and the NO_2/NO ratio rise progressively, suggesting a transition of the NO_x storage mechanism toward the nitrate pathway. This shift is attributed to the migration of stored nitrates from the catalyst surface into the bulk phase, or the spillover of NO_x species from Pt-proximal storage sites to more distant Ba-containing sites. As a result, leakage of NO and NO_2 gradually increases, and the catalyst approaches its NO_x storage saturation. The NO_2/NO ratio at this stage reflects the catalyst's ability to oxidize NO to NO_2.

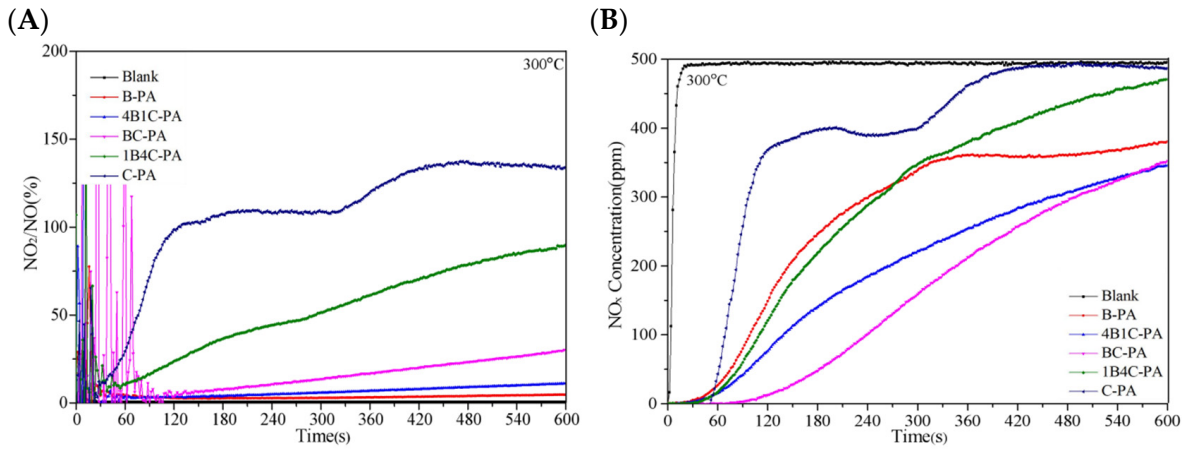


Figure 8. The (**A**) NO_2/NO and (**B**) NO_x Concentration Ratio Evolution during NO_x Storage over Catalysts with Different Ba/Ce Ratios at 300 °C.

Given the wide temperature range of vehicle exhaust gases, Table 4 summarizes the NO_x storage performance of fresh and hydrothermally aged catalysts with varying Ba/Ce ratios at four isothermal conditions: 200 °C, 300 °C, 400 °C, and 500 °C. As shown in the table, the NO_x storage capacity (NSC) of the fresh catalysts exhibits a volcano-type trend with respect to the Ba/Ce ratio. However, the optimal Ba/Ce ratio for storage varies with temperature. In the low-temperature range (200 °C and 300 °C), the NSC follows the order: BC-PA > 4B1C-PA > 1B4C-PA > B-PA > C-PA. In contrast, in the high-temperature range (400 °C and 500 °C), the order becomes: 4B1C-PA > B-PA > BC-PA > 1B4C-PA > C-PA. These trends suggest that Ce-containing species contribute more effectively to NO_x storage

at lower temperatures, while Ba-containing species are more active at elevated temperatures [39,40].

Table 4. NO_x Storage Performance of Catalysts with Different Ba/Ce Ratios at Various Temperatures.

Sample	200 °C		300 °C		400 °C		500 °C	
	NSC	NO_2/NO	NSC	NO_2/NO	NSC	NO_2/NO	NSC	NO_2/NO
	$mmol/g_{cat}$		$mmol/g_{cat}$		$(mmol/g_{cat})$		$mmol/g_{cat}$	
B-PA	148.59	0.90	239.35	4.73	280.21	21.90	162.50	11.21
4B1C-PA	199.83	3.00	317.81	10.94	328.30	29.70	164.68	11.13
BC-PA	228.85	5.50	361.27	30.20	278.92	34.94	137.32	11.50
1B4C-PA	165.96	15.13	216.81	89.90	109.28	37.71	40.74	11.31
C-PA	131.31	18.91	123.13	13.42	28.42	38.50	4.60	11.50
A-B-PA	64.73	11.93	36.31	23.83	32.69	28.95	16.42	11.30
A-4B1C-PA	91.28	10.95	73.51	34.80	68.86	33.11	41.34	11.62
A-BC-PA	82.42	12.91	47.20	34.91	43.58	34.62	23.01	11.81
A-1B4C-PA	81.94	15.46	40.43	56.49	28.13	35.75	7.92	11.50
A-C-PA	51.61	20.81	26.67	74.92	6.80	37.21	11.61	11.62

Comparing NO_x storage capacities at different temperatures reveals that high-Ba/low-Ce catalysts exhibit the highest NSC at 400 °C, whereas high-Ce/low-Ba catalysts perform best at 300 °C. This can be attributed to the lower thermal stability of stored nitrates with increasing Ce/Ba ratios, which is consistent with the NO_x-TPD results. After hydrothermal aging at 850 °C, the overall NO_x storage capacity of all catalysts is significantly reduced. Nevertheless, the volcano-type dependence on Ba/Ce ratio remains, indicating that an optimal Ba–Ce coexisting system enhances thermal durability—aligning well with the findings from pore structure and XRD analyses.

For both fresh and aged catalysts, the NO_2/NO activity increases with rising Ce/Ba ratios, indicating that the interfacial oxygen species at the Pt–CeO_2 interface play a crucial role in enhancing the oxidation capacity of the catalyst. Since the oxidation of NO to NO_2 is kinetically limited at low temperatures and thermodynamically constrained at high temperatures, a comparison of the NO_2/NO ratios at 200 °C reveals that aged catalysts exhibit superior oxidation performance. Based on the CO pulse adsorption and the semi-quantitative XRD particle size analysis, it can be inferred that larger Pt particles are more favorable for NO oxidation—a finding consistent with the study by Mulla et al. [41].

The NO_x storage performance of a catalyst depends not only on the basicity of the storage medium and the catalyst's ability to oxidize NO to NO_2, but more importantly, on the synergy between these two properties. Among the tested formulations, 4B1C-PA demonstrates practical application potential due to its strong NO oxidation ability, high NO_x storage capacity, and excellent hydrothermal stability.

2.8. Three-Way Catalytic Performance and Its Correlation with Catalyst Structure

Figure 9 presents the light-off performance of the catalysts under simulated rich–lean cycling conditions representative of practical TWC operation. As shown in the figure, for both fresh and aged samples, the light-off curves of CO, C_3H_6, and NO shift progressively toward higher temperatures with increasing Ba/Ce ratio, indicating that Ce-rich catalysts exhibit superior low-temperature activity due to their enhanced redox properties and oxygen mobility. In contrast, Ba-rich formulations show improved high-temperature conversion, consistent with the contribution of Ba-containing storage domains. The formation profiles of secondary species such as NH_3 and N_2O also shift to higher temperatures with

increasing Ba content, further reflecting the stronger redox functionality of Ce-rich catalysts at low temperatures and the increased H_2 availability that promotes NH_3 formation.

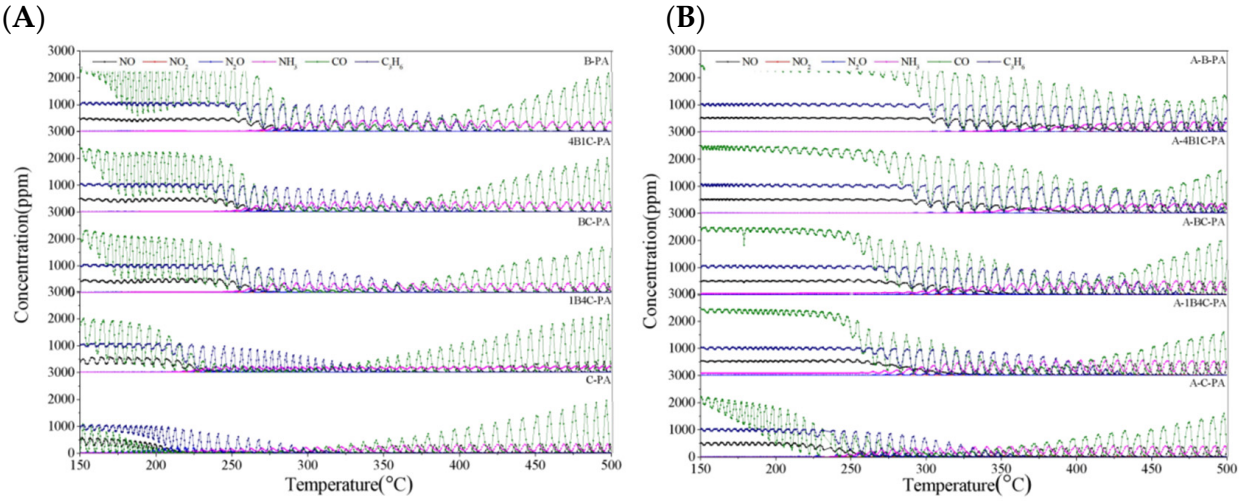


Figure 9. Dynamic Light-off Activity of (**A**) Fresh and (**B**) Hydrothermal Aging Catalysts with Varying Ba/Ce Ratios.

To evaluate catalytic activity under steady-state conditions, isothermal TWC measurements were performed at 200 °C and 500 °C, and the results are summarized in Tables 5 and 6. At 200 °C, the conversion efficiencies of NO_x, CO, and C_3H_6 increase with rising Ce content, accompanied by higher NH_3 and N_2O formation [12,42,43]. This trend highlights the ability of Ce-rich catalysts to participate in low-temperature redox, steam reforming, and water–gas shift reactions, thereby increasing the concentration of intermediate H_2 and promoting secondary product formation. Slight negative NO_x conversion values observed in some samples at low temperature arise from transient NO_x release rather than experimental artefacts. Specifically, thermally labile nitrate/nitrite species on $BaCO_3$- or CeO_2-associated sites can decompose during the early stages of light-off, and NO_2-to-NO back-reduction or oxygen-competition reactions during rich–lean switching may temporarily increase the outlet NO_x concentration above the inlet level. Such behavior is widely reported in LNT and TWC systems and is intrinsic to the dynamic NO_x storage–release process. In addition to NO_x conversion, the evolution of individual nitrogen-containing species (NO, NO_2, N_2O, NH_3, and N_2) was also analyzed to ensure the reliability of the catalytic performance. At low temperatures, Ce-rich catalysts exhibit increased NO_2 and N_2O formation due to their stronger oxidation capability and the involvement of Pt–CeO_2 interfacial oxygen. Meanwhile, the slight increase in outlet NO concentrations observed for some samples corresponds to the decomposition of surface nitrates/nitrites, consistent with the negative NO_x conversion values discussed above. NH_3 formation remains low at 200 °C but is detectable for Ce-rich catalysts, reflecting their ability to generate H_2 through low-temperature reforming and WGS pathways. Although N_2 is not directly measured, the nitrogen balance calculated as $N_2 = NO_{xin} - (NO + NO_2 + N_2O + NH_3)_{out}$ indicates that the majority of nitrogen is converted to N_2, with deviations within ±5% of the inlet nitrogen flux, confirming the internal consistency of the measurements and the absence of unaccounted nitrogen species.

At 500 °C, the overall NO_x conversion increases with the Ba/Ce ratio, whereas CO and C_3H_6 oxidation become less efficient for Ba-rich samples. These trends reinforce the distinct functional roles of the two promoters: Ba enhances high-temperature NO_x storage and regeneration capability, while Ce facilitates low-temperature oxidation pathways. The dependence of NH_3 formation on Ce loading further confirms the involvement of Ce-driven

redox and WGS chemistry in shaping the product distribution. At higher temperatures (500 °C), the evolution of nitrogen species reflects a shift toward complete reduction pathways. NO and NO_2 concentrations decrease substantially across all catalysts, while N_2O formation remains low, indicating efficient NO_x reduction in the presence of reductants generated from CO and hydrocarbon reforming. The calculated nitrogen balance shows that N_2 becomes the dominant product above 450 °C, with N_2 selectivity exceeding 85% for Ba-rich catalysts owing to their enhanced NO_x storage–reduction capability. Carbon balance analysis, based on the inlet and outlet CO and CO_2 concentrations, confirms that total carbon is conserved within ±3%, and no measurable methane or carbonaceous byproducts are detected. These results validate that the observed catalytic trends accurately represent the intrinsic reaction behavior of the Ba–Ce-modified Pt catalysts under TWC conditions.

Table 5. Three-Way Catalytic Activity of Catalysts with Different Ba/Ce Ratios at 200 °C.

Sample	Average NO_x Conversion (%)	Average CO Conversion (%)	Average C_3H_6 Conversion (%)	Average NH_3 Released (μmol $gcat^{-1}$ $cycle^{-1}$)	Average N_2O Released (μmol $gcat^{-1}$ $cycle^{-1}$)
B-PA	6.3	23.6	0.0	0.5	0.3
4B1C-PA	6.2	30.9	0.0	0.5	0.3
BC-PA	9.1	41.1	0.0	0.4	0.3
1B4C-PA	30.5	72.9	13.5	0.7	1.7
C-PA	75.4	98.8	36.2	1.5	7.4
A-B-PA	−0.8	−0.9	0.0	0.1	0.0
A-4B1C-PA	−2.1	0.2	0.0	0.1	0.0
A-BC-PA	−1.6	6.4	0.0	0.1	0.1
A-1B4C-PA	−3.6	23.1	0.0	0.7	0.1
A-C-PA	11.0	69.9	4.0	2.9	0.7

Table 6. Three-Way Catalytic Activity of Catalysts with Different Ba/Ce Ratios at 500 °C.

Sample	Average NO_x Conversion (%)	Average CO Conversion (%)	Average C_3H_6 Conversion (%)	Average NH_3 Released (μmol $gcat^{-1}$ $cycle^{-1}$)	Average N_2O Released (μmol $gcat^{-1}$ $cycle^{-1}$)
B-PA	96.5	59.5	100	7.9	0.0
4B1C-PA	92.3	52.3	100	8.0	0.0
BC-PA	85.2	64.5	100	6.8	0.0
1B4C-PA	72.9	60.9	100	4.8	0.0
C-PA	77.5	70.6	100	5.6	0.0
A-B-PA	66.4	65.9	69.4	7.3	0.0
A-4B1C-PA	66.6	56.0	91.9	9.0	0.0
A-BC-PA	59.8	49.5	100	11.1	0.0
A-1B4C-PA	57.6	57.2	100	10.9	0.0
A-C-PA	67.8	60.1	100	8.3	0.0

To elucidate the intrinsic correlation between the Ba/Ce ratio and the structural and catalytic performance of the catalysts, Figure 10A presents the variations in low-temperature average conversion efficiencies of NO_x, CO, and C_3H_6, as well as the specific surface area, pore volume, Pt particle size, and Pt/CeO_2 interfacial oxygen species content as functions of the Ba/Ce ratio. As shown in the figure, all these parameters exhibit linear trends with respect to the Ba/Ce ratio, indicating a close interrelationship among catalyst composition, structure, and performance.

During the catalyst preparation, Ba was introduced as a $Ba(CH_3COO)_2$ precursor, whereas Ce was added in the form of CeO_2 solid powder. With increasing Ba/Ce ratio,

the extent of pore blockage became more pronounced, leading to a decrease in specific surface area and pore volume, and a corresponding increase in Pt particle size. Conversely, a lower Ba/Ce ratio favored the efficient dispersion of Pt nanoparticles. The increased CeO_2 content enhanced the probability of Pt-CeO_2 contact, leading to a higher abundance of interfacial active oxygen species [36]. The efficient oxygen spillover facilitated by the Pt-CeO_2 interface accelerates the storage and release of oxygen, mitigating the impact of air-to-fuel ratio fluctuations on the three-way catalytic (TWC) performance. Additionally, the interfacial oxygen species contribute significantly to the activation and dissociation of gaseous pollutants, thereby improving the light-off performance of CO, NO_x, and C_3H_6 [44,45].

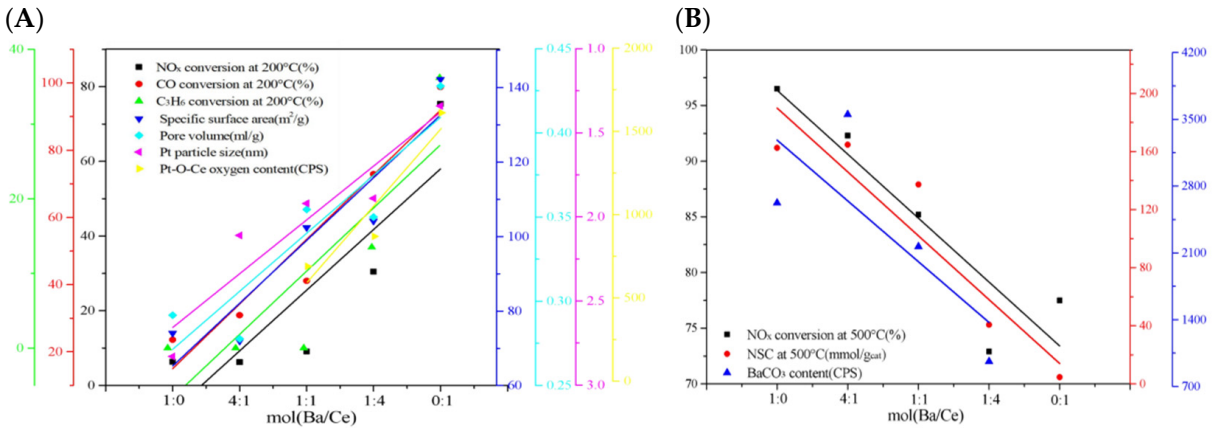


Figure 10. (**A**) Structure–Performance Correlation and (**B**) High-Temperature NO_x Conversion of Catalysts with Different Ba/Ce Ratios.

Given that the high-temperature NO_x conversion efficiency exhibits an opposite trend to that of CO and C_3H_6, Figure 10B further illustrates the relationship between the Ba/Ce ratio and the high-temperature average NO_x conversion efficiency, NO_x storage capacity, and $BaCO_3$ content. These parameters also show a near-linear relationship with the Ba/Ce ratio. With increasing Ba content, the $BaCO_3$ concentration increases, leading to enhanced NO_x storage capacity.

Under high-temperature conditions, water-gas shift and steam reforming reactions catalyzed by Pt induce deviations from the ideal air-fuel ratio (0.98–1.02), resulting in a generally leaner exhaust atmosphere [46]. Taking advantage of the inherent characteristics of lean NO_x storage and rich NO_x reduction, high-Ba catalysts exhibit superior NO_x conversion efficiency in high-temperature regimes.

Therefore, it can be inferred that coupling NO_x storage materials with conventional TWC catalysts to form NO_x storage-enabled TWC systems could effectively address the challenges of insufficient NO_x conversion performance during intermittent lean conditions and frequent thermal startups in aftertreatment systems.

3. Materials and Methods

3.1. Materials

Barium acetate ($Ba(CH_3COO)_2 \cdot H_2O$, analytical grade) was purchased from Xiya Chemical Technology Co., Ltd. (Zibo, Shandong, China). Cerium dioxide (CeO_2, industrial grade) was supplied by Panzhihua Sci-Resin Rare Earth New Materials Co., Ltd. (Panzhihua, China) Lanthanum-modified alumina (La_2O_3–Al_2O_3, industrial grade) was obtained from Weihai Fude New Materials Co., Ltd. (Weihai, China). The platinum precursor, diammine-dinitroplatinum(II) ($Pt(NH_3)_2(NO_2)_2$, industrial grade), was purchased from Guizhou Platinum Industry Co., Ltd. (Guiyang, China)

3.2. Catalyst Preparation

A platinum precursor solution was prepared by diluting 5 mL of an aqueous solution of diamminedinitroplatinum(II) ($Pt(NH_3)_2(NO_2)_2$, 100.12 g/L) with deionized water to a total volume of 100 mL. The solution was stirred at room temperature for 1 h. Subsequently, 35 g of La_2O_3–Al_2O_3 powder was added to the solution and stirred for an additional 10 min. Then, barium acetate and cerium dioxide were added sequentially in molar ratios of Ba/Ce = 1:0, 4:1, 1:1, 1:4, and 0:1, respectively, corresponding to different catalyst formulations. The resulting suspensions were continuously stirred at room temperature for 4 h.

After impregnation, the samples were dried overnight at 120 °C and subsequently calcined in static air at 600 °C for 4 h. The resulting fresh catalysts were designated as B-PA, 4B1C-PA, BC-PA, 1B4C-PA, and C-PA, corresponding to Ba/Ce molar ratios of 1:0, 4:1, 1:1, 1:4, and 0:1, respectively.

These fresh catalysts were subjected to hydrothermal aging at 850 °C for 10 h in a gas mixture of 8% H_2O, 8% O_2, 8% CO_2, and 76% N_2 at a total flow rate of 2 L/min. This accelerated aging protocol—commonly used to simulate the severe hydrothermal and oxidative environments encountered by TWCs during high-temperature engine operation—facilitates the evaluation of catalyst thermal stability and degradation pathways. The aged samples were denoted as A-B-PA, A-4B1C-PA, A-BC-PA, A-1B4C-PA, and A-C-PA, respectively.

3.3. Characterizations of Catalysts

To comprehensively investigate the physicochemical properties of the prepared catalysts and understand the structure–performance relationships, a series of characterization techniques were employed. Nitrogen physisorption analysis was conducted at 77 K to determine the specific surface area, pore volume, and pore size distribution via the Brunauer–Emmett–Teller (BET) method, providing insights into the textural properties of the catalysts. Powder X-ray diffraction (XRD) with Cu Kα radiation (λ = 0.154 nm) was used to identify the crystalline phases and to estimate the crystallite sizes of CeO_2, $BaCO_3$, and Pt species through Scherrer equation-based analysis. X-ray photoelectron spectroscopy (XPS) was employed to analyze the surface elemental composition and oxidation states, particularly the electronic interactions between Pt and the Ba/Ce-containing support. Scanning electron microscopy (SEM) was used to observe the surface morphology and microstructure of the catalyst layers. H_2 temperature-programmed reduction (H_2-TPR) was performed to assess the reducibility of metal oxides and to probe the strength of metal–support interactions. CO pulse chemisorption measurements were carried out to evaluate the dispersion of Pt species, allowing for estimation of surface metal area and average particle size. The actual Pt content in each sample was quantified by inductively coupled plasma optical emission spectroscopy (ICP-OES) following aqua regia digestion. Finally, NO_x temperature-programmed desorption (NO_x-TPD) analysis was conducted to study the NO_x storage capacity and desorption behavior, thereby elucidating the nature and strength of NO_x adsorption sites on the catalyst surface.

3.4. Catalytic Performance Evaluation

3.4.1. NO_x Storage Capacity (NSC) Evaluation

Isothermal NO_x storage performance was evaluated using a fixed-bed multifunctional catalyst testing system. In each test, 0.755 g of catalyst was loaded, and the gas hourly space velocity (GHSV) was maintained at 30,000 h^{-1}. Prior to NO_x adsorption, the catalyst was pretreated by heating to 550 °C in an oxidizing atmosphere containing 0.94 vol% O_2. Then, a reducing gas mixture of 2500 ppm CO and 1000 ppm C_3H_6 was introduced and maintained at 550 °C for 10 min. Afterward, the gas feed was switched back to the

oxidizing atmosphere (0.94 vol% O_2) and held for another 10 min. The system was then cooled to the desired storage temperature under the same oxidizing atmosphere.

The NO_x storage capacity (NSC) and the NO_2/NO ratio were calculated using the following equations:

$$NSC = \frac{1}{g_{cat} \cdot 22.4} \int_{t=0}^{t=600} V \cdot \left[C_{NO_x}^{blank} - C_{NO_x}^{out} \right] dt$$

$$\frac{NO_2}{NO} = \frac{C_{NO_2}^{out}}{C_{NO}^{out}} \times 100\%$$

where:

- NSC: NO_x storage capacity;
- g_{cat}: Mass of the catalyst sample (g);
- V: Total volumetric flow rate of the gas (L/min);
- $C_{NO_x}^{blank}$: NO_x concentration in the blank test (ppm);
- $C_{NO_x}^{out}$: NO_x concentration at the reactor outlet during storage (ppm);
- t: Time (min);
- 22.4: Molar volume of an ideal gas at standard temperature and pressure (L/mol);
- $C_{NO_2}^{out}$: Outlet concentration of NO_2 (ppm);
- C_{NO}^{out}: Outlet concentration of NO (ppm).

3.4.2. Three-Way Catalytic Performance Under Dynamic Light-Off Conditions

The dynamic light-off performance for three-way catalysis was evaluated using a fixed-bed multifunctional catalyst testing system. A catalyst sample of 0.755 g was used, and the gas hourly space velocity (GHSV) was set to 30,000 h^{-1}. The concentrations of the gas-phase products were continuously monitored using a Multigas 6000 on-line FTIR gas analyzer. The Multigas 6000 FTIR analyzer allows simultaneous quantification of NO, NO_2, N_2O, NH_3, CO, CO_2 and hydrocarbons, enabling continuous monitoring of all relevant gas-phase species during TWC evaluation. Prior to testing, the catalyst was pretreated by heating to 550 °C under a gas atmosphere containing 0.94 vol% O_2, 10 vol% H_2O, and 8 vol% CO_2, and held for 5 min. After pretreatment, the temperature was lowered to 150 °C, and a temperature-programmed reaction was conducted under rich-lean cycling conditions (λ = 0.98–1.02) with a switching frequency of 10 s. The temperature was ramped from 150 °C to 550 °C at a rate of 15 °C·min^{-1}. The detailed compositions of the feed gases during rich and lean phases are listed in Table 7.

Table 7. Reaction atmospheres.

Gas Composition	NO (ppm)	CO (ppm)	C_3H_6 (ppm)	CO_2 (%)	O_2 (%)	H_2O (%)	N_2	GHSV (h^{-1})
Lean	500	2500	1000	8	0.15	10	Balance gas	30,000
Rich	500	2500	1000	8	0.94	10	Balance gas	30,000

3.4.3. Steady-State Three-Way Catalytic Performance at Constant Temperature

The steady-state three-way catalytic (TWC) performance was evaluated using a fixed-bed multifunctional catalyst testing system. A catalyst mass of 0.755 g was employed, and the gas hourly space velocity (GHSV) was maintained at 30,000 h^{-1}. The outlet gas concentrations were continuously monitored using a Multigas 6000 on-line FTIR gas analyzer. Prior to testing, the catalyst was pretreated by heating to 550 °C under an oxidizing gas mixture containing 0.94 vol% O_2, 10 vol% H_2O, and 8 vol% CO_2, and held for 5 min. Then,

a reducing gas mixture containing 2500 ppm CO, 1000 ppm C_3H_6, 10 vol% H_2O, and 8 vol% CO_2 was introduced and maintained for 10 min. Afterward, the gas composition was switched back to the oxidizing mixture and held for another 10 min. The system was then cooled to the designated steady-state reaction temperature under the oxidizing atmosphere.

The TWC performance test was conducted at the steady-state temperature under rich-lean cycling conditions (λ = 0.98–1.02), with a switching frequency of 10 s. The detailed gas compositions for both rich and lean phases are listed in Table 1. Nitrogen (N_2) was used as the balance gas in all mixtures.

The average conversions of NO_x, CO, and C_3H_6, as well as the average NH_3 and N_2O formation, were calculated according to the following equations:

$$Average\ NO_X\ Conversion\ (\%) = \frac{\int_{t=0}^{t=190} V \cdot \left[C_{NO_X}^{blank} - C_{NO_X}^{out}\right] dt}{\int_{t=0}^{t=190} V \cdot C_{NO_X}^{blank} dt} \times 100\%$$

$$Average\ CO\ Conversion\ (\%) = \frac{\int_{t=0}^{t=190} V \cdot \left[C_{CO}^{blank} - C_{CO}^{out}\right] dt}{\int_{t=0}^{t=190} V \cdot C_{CO}^{blank} dt} \times 100\%$$

$$Average\ C_3H_6\ Conversion\ (\%) = \frac{\int_{t=0}^{t=190} V \cdot \left[C_{C_3H_6}^{blank} - C_{C_3H_6}^{out}\right] dt}{\int_{t=0}^{t=190} V \cdot C_{C_3H_6}^{blank} dt} \times 100\%$$

$$Average\ NH_3\ \ Released = \frac{Total\ mass\ of\ NH_3}{Catalyst\ mass \times Number\ of\ cycles}$$

$$Average\ N_2O\ \text{Released} = \frac{Total\ mass\ of\ N_2O}{Catalyst\ mass \times Number\ of\ cycles}$$

where:

- V: Total volumetric flow rate of the gas (L/min)
- C^{blank} : Pollutant concentration without the catalyst (ppm)
- C^{out} : Pollutant concentration at the reactor outlet (ppm)
- t: Time (s or min), integration period here is 190 s
- NH_3 or N_2O released: Measured by integrating NH_3 or N_2O signals over rich/lean cycles
- Total mass of N_2O: Integrated amount of N_2O measured over the test period
- Catalyst mass: Mass of catalyst used (g)
- Number of cycles: Total number of rich/lean switching cycles during the test

4. Conclusions

In this study, a series of Pt–Ba–Ce/Al_2O_3 catalysts with systematically varied Ba/Ce molar ratios were evaluated to elucidate how Ba–Ce compositional tuning governs structural evolution, redox behavior, NO_x storage, and three-way catalytic performance. Integrated characterization—BET, XRD, SEM, XPS, H_2-TPR, NO_x-TPD, CO pulse adsorption, and dynamic/steady-state TWC testing—reveals that the Ba/Ce ratio is a decisive parameter controlling Pt dispersion, interfacial Pt–CeO_2 oxygen species, $BaCO_3$ domain development, and their evolution under hydrothermal stress.

Catalysts with low Ba/Ce ratios exhibit higher surface areas, smaller Pt particles, and abundant Pt–O–Ce interfacial oxygen species, enabling efficient O_2 spillover and activation of CO, hydrocarbons, and NO_x at low temperatures. In contrast, Ba-rich catalysts promote the formation and enrichment of $BaCO_3$, yielding markedly enhanced NO_x storage capacity and superior high-temperature performance. As a result, the NO_x storage capacity displays a clear volcano-type dependence on Ba/Ce ratio, with Ce-rich compositions performing best at 200–300 °C and Ba-rich samples excelling at 400–500 °C.

Hydrothermal aging at 850 °C induces PtOx decomposition, Pt sintering, CeO_2 crystallite growth, and partial transformation of $BaCO_3$ into inert $BaAl_2O_4$. These processes diminish Pt–CeO_2 interactions, reduce oxygen mobility, and weaken NO_x storage efficiency. Nevertheless, catalysts with optimized Ba/Ce ratios effectively mitigate Pt sintering and preserve a larger fraction of active $BaCO_3$ domains, resulting in significantly improved structural and catalytic stability relative to Ba-rich or Ce-rich extremes.

Overall, this work establishes a mechanistic framework for understanding Ba–Ce cooperative effects in Pt-based catalysts and demonstrates, for the first time, that the Ba/Ce ratio simultaneously governs Pt–support interactions, oxygen spillover, NO_x storage chemistry, and hydrothermal durability. These findings provide actionable design guidelines for developing cost-effective, thermally robust Pt-based three-way catalysts as practical alternatives to Pd/Rh-dominated commercial formulations.

Author Contributions: Y.S., T.Z., L.G. and Y.H. contributed to catalyst synthesis, experimental assistance, and characterization measurements. J.D. assisted with data interpretation and provided technical support for catalytic testing. X.W. drafted the original manuscript. D.Y. and P.N. supervised the project, provided critical scientific guidance, and revised the manuscript. All authors discussed the results, commented on the manuscript, and approved the final version. All authors have read and agreed to the published version of the manuscript.

Funding: This work was supported by the National Key R&D Program of China (2024YFC3712402), the National Natural Science Foundation of China (22262016), the Major Science and Technology Project of Yunnan Province (202402AC080004), the Scientific and Technological Project of Yunnan Precious Metals Laboratory (YPML-20240502086), and the Technology Talents and Platform Project of Yunnan (202205AC160085).

Data Availability Statement: The data that support the findings of this study are available from the corresponding authors upon reasonable request.

Conflicts of Interest: Author Dongxia Yang, Yanxing Sun, Tingting Zheng, Lv Guo, Yao Huang and Junchen Du were employed by the company Kunming Sino-platinum Metals Catalysts Co. Ltd. The remaining authors declare that the research was conducted in the absence of any commercial or financial relationships that could be construed as a potential conflict of interest. The other authors declare that they have no known competing financial interests or personal relationships that could have appeared to influence the work reported in this paper.

References

1. Huang, C.; Shan, W.; Lian, Z. Catalysis Science & Technology Recent Advances in Three-Way Catalysts of Natural Gas Vehicles. *Catal. Sci. Technol.* **2020**, *10*, 6407–6419. [CrossRef]
2. Yin, X.; Li, S.; Deng, J.; Wang, Y.; Li, M.; Zhao, Y.; Wang, W.; Wang, J.; Chen, Y. Superior Pd–Rh Three-Way Catalyst: Modulating the Surface Composition by Introducing Ceria-Zirconia with Partial κ-Ce2Zr2O8 Structure as Support. *Ind. Eng. Chem. Res.* **2022**, *61*, 13011–13020. [CrossRef]
3. Wang, X.; Huang, C.; Wu, B.; Yang, W.; Zhang, Y.; Xu, Y.; Jiao, Y.; Zhong, L.; Wang, J. A Pt Catalyst with Enhanced Three-Way Catalytic Activity Supported on CeO_2 Modified with Al_2O_3 for Natural Gas Vehicles. *Ind. Eng. Chem. Res.* **2025**, *64*, 5854–5863. [CrossRef]
4. Su, Y.; Kabin, K.S.; Harold, M.P.; Amiridis, M.D. Reactor and in Situ FTIR Studies of Pt/BaO/Al_2O_3 and Pd/BaO/Al_2O_3 NO_x Storage and Reduction (NSR) Catalysts. *Appl. Catal. B Environ.* **2007**, *71*, 207–215. [CrossRef]
5. Casapu, M.; Grunwaldt, J.-D.; Maciejewski, M.; Krumeich, F.; Baiker, A.; Wittrock, M.; Eckhoff, S. Comparative Study of Structural Properties and NO_x Storage-Reduction Behavior of Pt/Ba/CeO_2 and Pt/Ba/Al_2O_3. *Appl. Catal. B Environ.* **2008**, *78*, 288–300. [CrossRef]
6. Lanza, A.; Bounechada, D.; Raphy, S.; Sato, R.; Phillipson, L.; Kolpin, A.; York, A.P.E. The Effect of the Oxygen Storage Material on a Three-Way Catalyst Spatio-Temporally Resolved with Spaci-MS. *Catal. Today* **2024**, *437*, 114775. [CrossRef]
7. Zhang, L.; Spezzati, G.; Muravev, V.; Verheijen, M.A.; Zijlstra, B.; Filot, I.A.W.; Su, Y.-Q.; Chang, M.-W.; Hensen, E.J.M. Improved Pd/CeO_2 Catalysts for Low-Temperature NO Reduction: Activation of CeO_2 Lattice Oxygen by Fe Doping. *ACS Catal.* **2021**, *11*, 5614–5627. [CrossRef]

8. Zhang, Y.; Yu, Y.; Shan, W.; Lian, Z.; He, H. Effect of Support Preparation with Different Concentration Precipitant on the NO_x Storage Performance of Pt/BaO/CeO_2 Catalysts. *Catal. Today* **2020**, *339*, 135–147. [CrossRef]
9. Wang, Y.; Zhao, Y.; Zhu, S.; Lu, J.; He, S.; Lu, H.; Song, D.; Luo, Y. Insight into the Effect of CeO_2 Morphology on Catalytic Performance for Steam Reforming of Glycerol. *Fuel* **2023**, *334*, 126587. [CrossRef]
10. Kanazawa, T. Development of Hydrocarbon Adsorbents, Oxygen Storage Materials for Three-Way Catalysts and NO_x Storage-Reduction Catalyst. *Catal. Today* **2004**, *96*, 171–177. [CrossRef]
11. Castoldi, L.; Nova, I.; Lietti, L.; Forzatti, P. Study of the Effect of Ba Loading for Catalytic Activity of Pt–Ba/Al_2O_3 Model Catalysts. *Catal. Today* **2004**, *96*, 43–52. [CrossRef]
12. Say, Z.; Vovk, E.I.; Bukhtiyarov, V.I.; Ozensoy, E. Influence of Ceria on the NO_x Reduction Performance of NO_x Storage Reduction Catalysts. *Appl. Catal. B Environ.* **2013**, *142–143*, 89–100. [CrossRef]
13. Peden, C.H.F.; Kim, D.H.; Chin, Y.; Kwak, J.H. Changes in Ba Phases in BaO/Al_2O_3 upon Thermal Aging and H_2O Treatment. *Catal. Lett.* **2005**, *105*, 259–268. [CrossRef]
14. Zhang, L.; Bao, Q.; Zhang, B.; Zhang, Y.; Wan, S.; Wang, S.; Lin, J.; Xiong, H.; Mei, D.; Wang, Y. Distinct Role of Surface Hydroxyls in Single-Atom Pt1/CeO_2 Catalyst for Room-Temperature Formaldehyde Oxidation: Acid–Base Versus Redox. *JACS Au* **2022**, *2*, 1651–1660. [CrossRef]
15. Kim, B.-S.; Kim, P.S.; Bae, J.; Jeong, H.; Kim, C.H.; Lee, H. Synergistic Effect of Cu/CeO(2) and Pt-BaO/CeO(2) Catalysts for a Low-Temperature Lean NO (x) Trap. *Environ. Sci. Technol.* **2019**, *53*, 2900–2907. [CrossRef]
16. Thommes, M.; Kaneko, K.; Neimark, A.V.; Olivier, J.P.; Rodriguez-Reinoso, F.; Rouquerol, J.; Sing, K.S.W. Physisorption of Gases, with Special Reference to the Evaluation of Surface Area and Pore Size Distribution (IUPAC Technical Report). *Pure Appl. Chem.* **2015**, *87*, 1051–1069. [CrossRef]
17. Cychosz, K.A.; Thommes, M. Progress in the Physisorption Characterization of Nanoporous Gas Storage Materials. *Engineering* **2018**, *4*, 559–566. [CrossRef]
18. Chen, X.; Chen, J.; Zhao, Y.; Chen, M.; Wan, H. Effect of Dispersion on Catalytic Performance of Supported Pt Catalysts for CO Oxidation. *Chinese J. Catal.* **2012**, *33*, 1901–1905. [CrossRef]
19. Shen, M.; Lv, L.; Wang, J.; Zhu, J.; Huang, Y.; Wang, J. Study of Pt Dispersion on Ce Based Supports and the Influence on the CO Oxidation Reaction. *Chem. Eng. J.* **2014**, *255*, 40–48. [CrossRef]
20. Swartz, S.L. Catalysis by Ceria and Related Materials Edited by Alessandro Trovarelli (Università di Udine, Italy). Catalytic Science Series. Volume 2. Series Edited by Graham J. Hutchings. Imperial College Press: London. 2002. vviii + 508 pp. $78.00. ISBN: 1-86094-299-7. *J. Am. Chem. Soc.* **2002**, *124*, 12923–12924. [CrossRef]
21. Zhang, T.; Zheng, T.; Yang, K.; Dai, X.; Guo, L.; Yang, D.; Chang, S.; Wang, C.; Zhao, Y. Improving the Catalytic Activity and Thermal Stability of Pt-Supported Catalyst via Modulating Ce/Zr Molar Ratio. *Appl. Surf. Sci.* **2024**, *670*, 160689. [CrossRef]
22. Aneggi, E.; Boaro, M.; Colussi, S.; de Leitenburg, C.; Trovarelli, A. Chapter 289—Ceria-Based Materials in Catalysis: Historical Perspective and Future Trends. In *Including Actinides*; Bünzli, J.-C.G., Pecharsky, V.K., Eds.; Handbook on the Physics and Chemistry of Rare Earths; Elsevier: Amsterdam, The Netherlands, 2016; Volume 50, pp. 209–242. [CrossRef]
23. Feng, J.; Gao, C.; Yin, Y. Stabilization of noble metal nanostructures for catalysis and sensing. *Nanoscale* **2018**, *10*, 20492–20504. [CrossRef] [PubMed]
24. Wang, Q.; Ling, W.; Lu, Y.; Zhao, H.; Cheng, Q.; Huang, Y. Synergistic Stabilization of Pt Single Atoms by Cl and Ru for Industrial-Scale Current Density Hydrogen Production. *Angew. Chem. Int. Ed. Engl.* **2025**, *64*, 202506619. [CrossRef] [PubMed]
25. Liu, W.; Flytzanistephanopoulos, M. Total Oxidation of Carbon Monoxide and Methane over Transition Metal Fluorite Oxide Composite Catalysts: I. Catalyst Composition and Activity. *J. Catal.* **1995**, *153*, 304–316. [CrossRef]
26. Wu, Z.; Li, M.; Overbury, S.H. On the Structure Dependence of CO Oxidation over CeO_2 Nanocrystals with Well-Defined Surface Planes. *J. Catal.* **2012**, *285*, 61–73. [CrossRef]
27. Castro-Latorre, P.; Neyman, K.M.; Bruix, A. Systematic Characterization of Electronic Metal—Support Interactions in Ceria-Supported Pt Particles. *J. Phys. Chem. C* **2023**, *127*, 17700–17710. [CrossRef]
28. Slavinskaya, E.M.; Stadnichenko, A.I.; Domínguez, J.E.Q.; Stonkus, O.A.; Vorokhta, M.; Šmíd, B.; Castro-Latorre, P.; Bruix, A.; Neyman, K.M.; Boronin, A.I. States of Pt/CeO_2 Catalysts for CO Oxidation below Room Temperature. *J. Catal.* **2023**, *421*, 285–299. [CrossRef]
29. Aneggi, E.; Wiater, D.; de Leitenburg, C.; Llorca, J.; Trovarelli, A. Shape-Dependent Activity of Ceria in Soot Combustion. *ACS Catal.* **2014**, *4*, 172–181. [CrossRef]
30. Jan, A.; Shin, J.; Ahn, J.; Yang, S.; Yoon, J.; Son, J.; Kim, H.; Lee, J.; Ji, H. Promotion of Pt/CeO_2 Catalyst by Hydrogen Treatment for Low-Temperature CO Oxidation. *RSC Adv.* **2019**, *9*, 27002–27012. [CrossRef]
31. Ferré, G.; Aouine, M.; Bosselet, F.; Burel, L.; Aires, F.J.C.S.; Geantet, C.; Ntais, S.; Maurer, F.; Casapu, M.; Grunwaldt, J.; et al. Catalysis Science & Technology for Low-Temperature CO Oxidation. *Catal. Sci. Technol.* **2020**, *10*, 3904–3917. [CrossRef]
32. Stadnichenko, A.I.; Slavinskaya, E.M.; Stonkus, O.A.; Boronin, A.I. Low-Temperature CO Oxidation by the Pt/CeO_2 Based Catalysts. *ChemCatChem* **2024**, *16*, e202301727. [CrossRef]

33. Vincent, J.L.; Crozier, P.A. CeO_2 -Supported Pt Catalysts for CO Oxidation. *Nat. Commun.* **2021**, *12*, 5789. [CrossRef] [PubMed]
34. Wang, Z.; Wang, Y.; Subramanian, M.A.; Jiang, P. Structure and Functional Properties of Oxides in the BaO–Al_2O_3 System: Phosphors, Pigments and Catalysts. *Prog. Solid State Chem.* **2022**, *68*, 100379. [CrossRef]
35. Wang, T.; Jia, L.-W.; Wang, X.-T.; Wang, G.; Luo, F.-Q.; Wang, J.-M. Enhancing Low-Temperature NO_x Storage and Reduction Performance of a Pt-Based Lean NO_x Trap Catalyst. *Rare Met.* **2019**, *38*, 81–86. [CrossRef]
36. Clayton, R.D.; Harold, M.P.; Balakotaiah, V.; Wan, C.Z. Pt Dispersion Effects during NO_x Storage and Reduction on Pt/BaO/Al_2O_3 Catalysts. *Appl. Catal. B Environ.* **2009**, *90*, 662–676. [CrossRef]
37. Seo, C.-K.; Kim, H.; Choi, B.; Lim, M.T.; Lee, C.-H.; Lee, C.-B. De-NO_x Characteristics of a Combined System of LNT and SCR Catalysts According to Hydrothermal Aging and Sulfur Poisoning. *Catal. Today* **2011**, *164*, 507–514. [CrossRef]
38. Liu, Z.; Epling, W.S.; Anderson, J.A. Influence of Pt Loading in Aged NO_x Storage and Reduction Catalysts. *J. Phys. Chem. C* **2011**, *115*, 952–960. [CrossRef]
39. Shi, C.; Ji, Y.; Graham, U.M.; Jacobs, G.; Crocker, M.; Zhang, Z.; Wang, Y.; Toops, T.J. NO_x Storage and Reduction Properties of Model Ceria-Based Lean NO_x Trap Catalysts. *Appl. Catal. B Environ.* **2012**, *119–120*, 183–196. [CrossRef]
40. Symalla, M.O.; Drochner, A.; Vogel, H.; Büchel, R.; Pratsinis, S.E.; Baiker, A. Structure and NO_x Storage Behaviour of Flame-Made $BaCO_3$ and Pt/$BaCO_3$ Nanoparticles. *Appl. Catal. B Environ.* **2009**, *89*, 41–48. [CrossRef]
41. Mulla, S.S.; Chen, N.; Cumaranatunge, L.; Blau, G.E.; Zemlyanov, D.Y.; Delgass, W.N.; Epling, W.S.; Ribeiro, F.H. Reaction of NO and O_2 to NO_2 on Pt: Kinetics and Catalyst Deactivation. *J. Catal.* **2006**, *241*, 389–399. [CrossRef]
42. Hilaire, S.; Wang, X.; Luo, T.; Gorte, R.J.; Wagner, J. A Comparative Study of Water-Gas-Shift Reaction over Ceria Supported Metallic Catalysts. *Appl. Catal. A Gen.* **2001**, *215*, 271–278. [CrossRef]
43. Panagiotopoulou, P.; Kondarides, D.I. Effect of the Nature of the Support on the Catalytic Performance of Noble Metal Catalysts for the Water–Gas Shift Reaction. *Catal. Today* **2006**, *112*, 49–52. [CrossRef]
44. Wang, C.; Feng, F.; Du, J.; Zheng, T.; Pan, Z.; Zhao, Y. Activation of Surface Lattice Oxygen in Ceria Supported Pt/Al_2O_3 Catalyst for Low-Temperature Propane Oxidation. *ChemCatChem* **2019**, *11*, 2021. [CrossRef]
45. Chen, D.; He, D.; Lu, J.; Zhong, L.; Liu, F.; Liu, J.; Yu, J.; Wan, G.; He, S.; Luo, Y. Investigation of the Role of Surface Lattice Oxygen and Bulk Lattice Oxygen Migration of Cerium-Based Oxygen Carriers: XPS and Designed H2-TPR Characterization. *Appl. Catal. B Environ.* **2017**, *218*, 249–259. [CrossRef]
46. Zhou, Z.; Harold, M.P.; Luss, D. Comparison of Pt-BaO/Al_2O_3 and Pt-CeO_2/Al_2O_3 for NO_x Storage and Reduction: Impact of Cycling Frequency. *Appl. Catal. B Environ.* **2019**, *255*, 117742. [CrossRef]

Disclaimer/Publisher's Note: The statements, opinions and data contained in all publications are solely those of the individual author(s) and contributor(s) and not of MDPI and/or the editor(s). MDPI and/or the editor(s) disclaim responsibility for any injury to people or property resulting from any ideas, methods, instructions or products referred to in the content.